Using 2d Infrared Imaging for the Analysis of Non-Conventional Fuels Combustion in a Diesel Engine

E.Mancaruso, B.M.Vaglieco, L.Sequino

Abstract

The common realization of the necessity to reduce the use of mineral sources is promoting the use of alternative fuels. Big efforts are being made to replace petroleum derivatives in the internal combustion engines (ICEs). For this purpose it is mandatory to evaluate the behavior of non-conventional fuels in the ICEs.
The optical diagnostics have proven to be a powerful tool to analyze the processes that take place inside the engine. In particular, 2d imaging in the infrared range can reveal new details about the effect of the fuel properties since this technique is still not very common.
In this work, a comparison between commercial diesel fuel and two non-conventional fuels has been made in an optically accessible diesel engine. The non-conventional fuels are: the first generation biofuel Rapeseed Methyl Ester (RME) and an experimental blend of diesel and a fuel with high glycerol content (HG). Both a CCD visible camera and an infrared camera have been used to record images from the combustion chamber. The infrared range investigated is from 1.5 to 5 μm; moreover, a band pass filter at 4.2 μm has been used to impress the radiation of the CO_2 molecules while a filter at 3.9 μm has been used to visualize the fuel location in terms of HCs, and the reacting spray by intermediate products of the combustion process. The engine mounts the head of a real Euro5 diesel engine and a Common Rail injection system with solenoid injector. The engine head is placed on an elongated piston and an optical access in the piston provides the bottom view of the combustion chamber. Images are taken by means of a 45° IR-mirror located in the elongated piston. The engine runs in two operating points of the New European Driving Cycle in order to investigate the mixing process in conditions similar to those of the real engine.
The infrared imaging has proven to give important information about the in-cylinder reactions. The pilot injection vaporization and mixing has been evaluated. The interaction between the main injection and the reacting fuel has been analyzed. Finally, CO_2 plumes appear at the end of main injection and they are isolated on the tip of the jets and close to the chamber wall.

Introduction

The compression ignition (CI) engine is the most common propeller for civil and commercial transport. In the last years CI engines have been strongly improved to reduce pollutant emissions and fuel consumption. In order to meet these requirements various modifications in the engine hardware have been made and different alternative fuels have been used. In order to reduce the crude oil dependency, the research for renewable fuel sources has led to an increasing use of biodiesel. The first generation biodiesel includes a wide range of methyl ester blends produced from vegetable oils and animal fats through the thermo-chemical process of transesterification [1]. Several studies have been made to evaluate the effects of biodiesel on the performances and exhaust emissions of a CI engine [2, 3, 4]. For example, the lower heating value (LHV) of biodiesel is lower than diesel and this produces less torque related to diesel fuel at fixed injection strategy [5]. Biodiesel could be a cleaner fuel for ICEs compared to the diesel one. Engines fuelled with biofuels emit lower carbon monoxide (CO), hydrocarbon (HC) and particulate matter (PM) [6]. As a result of the increasing biofuel production, also the production of glycerol, which is the main by-product of the transesterification process, is grown. Using the glycerol surplus as alternative fuel in ICEs would be the best solution. Unfortunately, because of its detrimental physical and chemical properties, raw glycerol is not suitable as alternative fuel in ICEs. Studies from literature [7] have proven its potential use as fuel additive. Blends of diesel/biodiesel and oxygenated compounds derived from glycerol etherification can improve engine performance and reduce PM, HC, CO and unregulated aldehydes emission [8]. In particular, blends with ethers of glycerol can improve the low temperature properties for diesel fuel and reduce the viscosity for biodiesel fuel.

Complex technologies are used to monitor the processes involved in the ICEs. Optical diagnostics provide considerable insight for the development of modern engines. While the investigation of the infrared (IR) spectrum has been performed mainly by means of spectroscopic emission [9, 10], 2d infrared imaging is still not very common. In previous works [11, 12, 13], authors set up an IR camera to analyze the combustion process in an optically accessible diesel engine. The tests pointed out the potential of this technique and the need for further investigations.

The aim of the present work is to make a comparative analysis of the combustion process in a diesel engine fuelled with non-conventional fuels by means of 2d infrared imaging. The non-conventional fuels are: the first generation biofuel Rapeseed Methyl Ester (RME) [14, 15] and an experimental blend of diesel and a fuel with high glycerol content (HG) [16]. For the acquisition of in-cylinder images both a charge coupled device (CCD) visible camera and an IR camera have been used. The infrared range investigated is from 1.5 to 5 μm; moreover a band pass filter at 4.2 μm has been used to impress the radiation of the CO_2 molecules [17] while a filter at 3.9 μm has been used to visualize the fuel location in terms of HCs and the reacting spray by intermediate products of the combustion process [18]. The optical engine mounts the head of a real Euro5 diesel engine and a Common Rail injection system with solenoid injector. The engine head is placed on an elongated piston and an optical access in the piston provides the bottom view of the combustion chamber. Images are taken by means of a 45° IR-mirror located in the elongated piston.

The engine has been run in two operating points of the New European Driving Cycle characterized by a double injection strategy in conditions similar to those of the real engine. The imaging analysis in the infrared range has given important information about the effect of fuel properties on combustion reactions.

Experimental apparatus and procedures

Optical engine

The optical single-cylinder engine used for combustion diagnostics was equipped with the combustion system architecture and injection system of a Euro5 compliant four cylinders engine. The single-cylinder engine lay-out is shown in Figure 1. Moreover, the engine specifications are reported in Table 1.

The optical engine utilized a conventionally extended piston with a piston crown window of 46 mm diameter which provided full view of the combustion bowl by locating an appropriate 45° fixed IR-visible mirror inside the extended piston. Even if the bowl bottom is flat, the combustion bowl volume and the bowl wall shape were kept the same as the production engine by reducing the bowl bottom distance. Figure 2 shows the original and modified combustion chamber. Since the heat conductivity of sapphire is about 5 times lower than that of aluminum while the one of the quartz is about 100 times lower than the aluminum [19], the window was made of sapphire to minimize the heat release differences between metal and optical engine [20]. To match the in-cylinder conditions of the multi-cylinder engine tests, an external air compressor was used to supply pressurized intake air that was filtered and dehumidified. Thanks to the dehumidification, the measure of the air mass flow, depending on the volume flow, the pressure and the temperature, is not affected by the uncertainties related to the presence of water. Then, the air was heated up to a desired inlet temperature that ensures the same rate of heat release of the metal engine [20, 21]. A reliable measure of the air mass flow before the mixing with the recirculated gases allows calculating the effective recirculation of exhaust gases (EGR) percentage. The engine was also equipped with a Common Rail injection system managed by a fully opened electronic control unit (ECU). The ECU allowed controlling the number of injections per cycle, the injection pressure, the injection start, the energizing time that manage the injector as well as the dwell time between two consecutive injections. A solenoid driven injector was used, more specifications about the injection system have been reported in Table 2.To analyze the current profile, a Hall-effect sensor was applied to the line of the solenoid of the injection. Moreover, to record the in-cylinder pressure in motored and fired condition, a piezoelectric pressure transducer (AVL GH13P) was set in the glow plug seat of the engine head.

Table 1. Optical engine characteristics.

Engine type	4-stroke single cylinder
Bore	85 mm
Stroke	92 mm
Swept volume	522 cm^3
Combustion bowl	19.7 cm^3
Vol. compression ratio	16.5:1

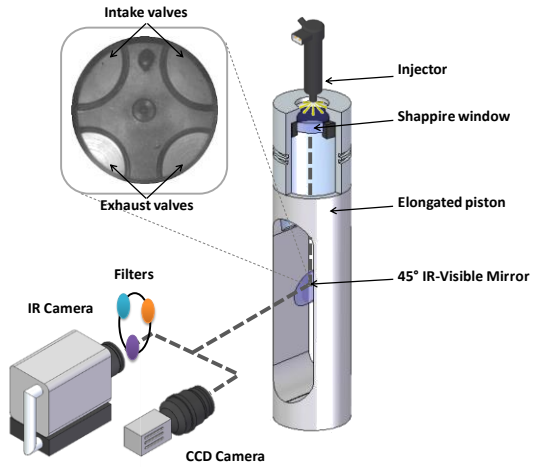

Figure 1. Single-cylinder engine optical setup.

Table 2. Injection system characteristics.

Injection system	Common Rail
Injector type	Solenoid driven
Number of holes	7
Spreading angle of fuel jet axis	148°
Hole diameter [µm]	141

Figure 2. Original (left) and modified (right) geometry of the combustion chamber.

For each operating condition investigated, the cylinder pressure and the signal of the drive injector current were digitized and recorded at 0.1 crank angle degree (°CA) increments and ensemble-averaged over 150 consecutive combustion cycles. Moreover, the cyclic variation was measured and it resulted less than 1% with respect to the maximum pressure and less than 3% with respect to the indicated mean effective pressure (IMEP). The heat release rate was calculated from the ensemble-averaged pressure data using the first law of thermodynamics and the perfect gas model [22].

Optical setup

Visible imaging

In Figure 1, a scheme of the optical setup has been reported. Visible imaging analysis was performed by a charge coupled device (CCD) camera through the 45° mirror. The camera used is the PixelFly VGA COLOR; it has 640 x 480 pixels (pixel dimensions of 9.9 x 9.9 μm^2) and a high sensitivity over a wide visible range. It was used in order to take images during the injection and combustion processes. A visible lens, Nikkor 55 mm f/3.5, was used. Due to speed limitation

of CCD camera, only one image was recorded in a given cycle. The size of the images was 460x460 pixels with a resolution of 0.1 mm per pixel. The spray parameters were investigated by means of two halogen continuous lamps that lighted the jets in the bowl via the 45° mirror. During both the pilot and main events several images from separate cycles were recorded up to the end of visible injection. For the measurement of the spray global quantities, five repetitions were performed. The number of repetitions is limited by the fouling of the sapphire window; however, test performed with a cycle resolved camera have shown a low cycle to cycle variability of the injection process. No lamps were used to record the combustion phase because of the luminosity of the flames. The synchronization of the CCD camera with the engine was obtained by a delay unit connected with the signal coming from the engine shaft encoder. The synchronization system could be adjusted to obtain single images at a desired crank angle. In particular, the images were recorded with an exposure time of 55 μs and 41 μs that corresponded to 0.5°CA of the shaft encoder at 1500 rpm and 2000 rpm, respectively. In order to evaluate the in-cylinder soot for each crank angle, two-color pyrometry has been performed using the software AVL Visioscope. The analysis has been made on color images of the combustion event using the red and green channels of the CCD camera [23].

Infrared imaging

IR imaging was performed using the FLIR Phoenix fast camera (320×256 pixels) able to detect light in the range 1.5-5 μm. The IR camera had a sensor made of Indium Antimonide and it was equipped with a 25 mm lens, f/2.3. The cycle resolved camera was used at 3003 Hz that corresponds to an angular step of 3°CA and 4°CA, at 1500 rpm and 2000 rpm, respectively. The size of the images was 128x49 pixels with a resolution of 1.1 mm per pixel. Images from IR camera were detected with an exposure time of 10 μs. However, it was necessary to use a Neutral Density filter with 10% attenuation (ND1) to prevent the saturation of the detected images. Moreover, two band pass filters at 3.9 μm and 4.2 μm have been used; their bandwidth is ± 150 nm.

The spectral range of the IR camera is quite wide (1.5-5 μm). Several species related to the combustion process emit in this band, e.g. CO, CO_2, CH, OH, H_2O et al. [18]. Beside the collection of the IR emission in the whole camera range, two band pass filters have been selected to visualize single chemical species. Since the asymmetric stretch vibrational mode of the CO_2 molecule correspond to wavelength 4.2 μm [17], a band pass filter at this wavelength has been used to visualize the in-cylinder distribution of CO_2. The second band pass filter used is at the wavelength 3.9 μm.
From the chemical point of view, the wavelength 3.9 μm corresponds to the wavenumber 2564 cm^{-1}. This is not characteristic of a particular species; however it is affected by the presence of other species whose signal is centered close to 2564 cm^{-1}. For example, the range 3300-2500 cm^{-1} is where acid OH emits (center at 3000cm^{-1}). The OH peaks due to carboxylic acids (COOH) show a very broad and less intense peak between 2500 and 3500 cm^{-1}. The alkyl C-H has a peak between 3000 and 2800 cm^{-1}. And the aldehyde C-H has two medium intensity peaks on the right hand shoulder of the alkyl C-H's (2850 and 2750 cm^{-1}) [18]. Hence, the band pass filter at 3.9 μm has been used to visualize HCs and the intermediate products of the combustion reactions.

Fuels

Diesel fuel has been used as reference fuel; in addition, two non-conventional fuels have been tested to analyze the advantages of using alternative fuel in a modern diesel engine. The first non-conventional fuel is pure Rapeseed Methyl Ester (RME), a first generation biofuel derived from edible oil. The second one, denoted as HG, is a blend of commercial diesel fuel (80% v/v) and an experimental fuel with high glycerol content (20% v/v) obtained from etherification of glycerol with tert-butyl alcohol and isobutylene [24]. Properties of the tested fuels have been reported in Table 3.

Engine operating conditions

The data presented in this paper were taken with the optical engine operating in continuous mode. The engine operating conditions investigated were representative of the engine behavior installed on a D-class vehicle during the New European Driving Cycle (NEDC). They corresponded to the calibration points at 1500 rpm at 2 bar of brake mean effective pressure (BMEP) and 2000 rpm at 5 bar of BMEP; hereafter referred to as “1500x2” and “2000x5”, respectively. A collection of engine load/speed values recorded during the NEDC has been reported in Figure 3. The engine operating conditions selected for this work correspond to the red dots. In motored conditions, temperature and density at Top Dead Center (TDC) were estimated assuming the pressure at the bottom dead center (BDC) equal to the intake manifold pressure and a polytropic transformation with a coefficient of 1.36 [22]. This value was chosen after a validation procedure considering a sample of motored data at different intake pressures and engine speeds. Starting from the intake pressure, the pressure at the TDC was calculated using the polytropic transformation. The calculated value was compared to the one measured by the pressure transducer. Using the exponent 1.36, errors were inside the range ±3%. Finally, since no significant differences in the calculated ROHR curve were observed across the TDC using lower values of the polytropic exponent, the exponent value 1.36 was adopted for the calculation of the temperature and density at the TDC. The absolute intake air pressure and temperature, the in-cylinder temperature and density at the TDC in motored conditions have been reported in Table 4. The injection strategies consisted of two events per cycle, pilot and main; the injection pressure for each engine point has been reported in Table 4. Since the engine is operated in continuous mode, true recirculation of exhaust gases (EGR) was performed using the hot gases of each combustion cycle. The EGR is used in order to reduce the emission of nitrogen oxides (NOx); values used for each engine operating point have been reported in Table 4.
Figure 4 reports the combustion signals of the two selected operating points (1500x2 and 2000x5) for the reference fuel. In particular, the pressure signal, the calculated rate of heat release (ROHR), and the injector current have been reported for the optical engine (solid line with symbols) and the real engine (dashed line). The current signals are the same for both engines since the same injection strategies have been used.

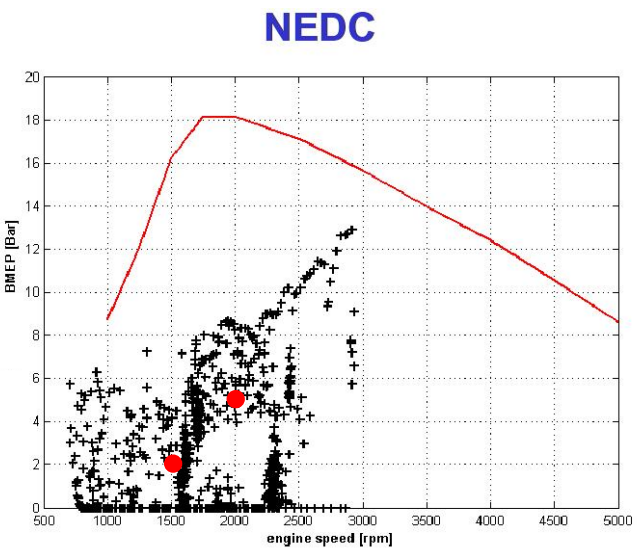

Figure 3. Load-speed diagram of the NEDC. The red line is the engine operating limit. The red dots correspond to the two engine operating condition investigated.

Table 3. Fuel properties.

Feature/Method	**Units**	**Commercial Diesel**	**HG**	**RME**
Density @ 15 °C (EN ISO 12185)	***[kg/m³]***	829	838	882
Cetane Number (EN ISO 5165)	***[-]***	51.8	46.5	53.1
Low Heating Value (ASTM D3338)	***[MJ/kg]***	42.4	40.3	37.4
Flash Point (ASTM D93/IP 34/ EN ISO 2719)	***[°C]***	72	52	-
Kinematic Viscosity 40°C (ASTM D445)	***[mm²/s]***	2.7	3.3	4.5
Cloud Point (ASTM D2500)	***[°C]***	-2.2	-2	-2/1
Cold Filter Plugging Point (EN 116)	***[°C]***	-19	-18	-10
Lubricity 60°C (ISO 12156-1)	***[µm]***	382	235	119
Distillation (ASTM D86)	***IBP [°C]***	159	146	316
	10%vol. [°C]	194	196	347
	50%vol. [°C]	268	255	350
	90%vol. [°C]	333	308	353
	95%vol. [°C]	350	321	356
	FBP [°C]	361	330	365
Carbon (ASTM D5991)	***[mol%]***	~85.5	~79.9	~77.8
Hydrogen (ASTM D5991)	***[mol%]***	~13.5	~11.9	~11.4
Oxygen (ASTM D5991)	***[mol%]***	~1.4	~8.2	~10.4

Table 4. Parameters of the engine operating conditions.

Operating Condition	Absolute intake air pressure [bar]	Intake air temperature [°C]	Temp @ TDC [°C]	Density @ TDC [kg/m³]	Injection pressure [bar]	EGR [%]
1500x2	1.25	48	551	18.6	615	58
2000x5	1.42	60	581	20.3	891	29

Table 5. Injection strategies.

Operating Condition	SOI Pilot [°CA]	ET Pilot [µs]	SOI Main [°CA]	ET Main [µs]	Start/End of Pilot injection from visible images [°CA]	Start/End of Main injection from visible images [°CA]
1500x2	-15.8	290	-5.8	545	-13/-11	-3.5/2
2000x5	-18.6	257	-2.4	560	-15/-12.5	1.5/9

The injection strategies have been reported in Table 5. It reports also the effective start/end of injection detected from the visible images. The delay between the start of injection (SOI) from the ECU and the effective SOI has been calculated and it is around 300 µs for all the injections and engine conditions. In both operating points, the pressure values at the top dead center (TDC) in the optical engine are close to the real engine ones. This fit has been obtained using higher intake pressures in the optical engine to compensate for its blow-by losses and lower compression ratio (CR). The effect of higher intake pressure is evident in Figure 4; the pressure trace of the optical engine is the highest during the compression stroke. The low CR is also responsible for the low peak pressure in the optical engine. The main target was to overlap the ROHR trace in order to reproduce the same combustion behavior [20, 25]. Figure 4 shows a good fit of the ROHR curves of real and optical engines. By managing the intake temperatures, it was possible to match the SOC of the optical engine with the real engine one. The combustion of the pilot injection releases a small quantity of energy; it generates a local peak with low intensity. On the other hand, the combustion of the main injection releases the main energy and it is characterized by a fast increase of heat release typical of premixed combustion. At 1500x2, the slope of the ROHR trace is the same for optical and real engine and the two peaks overlap; this indicates that the same combustion rate has been reached. On the contrary, at 2000x5, the peak of the ROHR is reached earlier in the optical engine denoting a faster combustion. Increasing the engine speed, the combustion frequency increases, and hence the in-cylinder temperature increases too. For the optical engine, the temperature is higher than in the real engine due to lower heat conductivity of optical parts, and this promotes combustion reactions. Finally, optical engine demonstrated to reproduce the combustion cycle of the real engine in a reliable way. And this is mandatory for the analysis of in-cylinder processes by means of optical diagnostics.

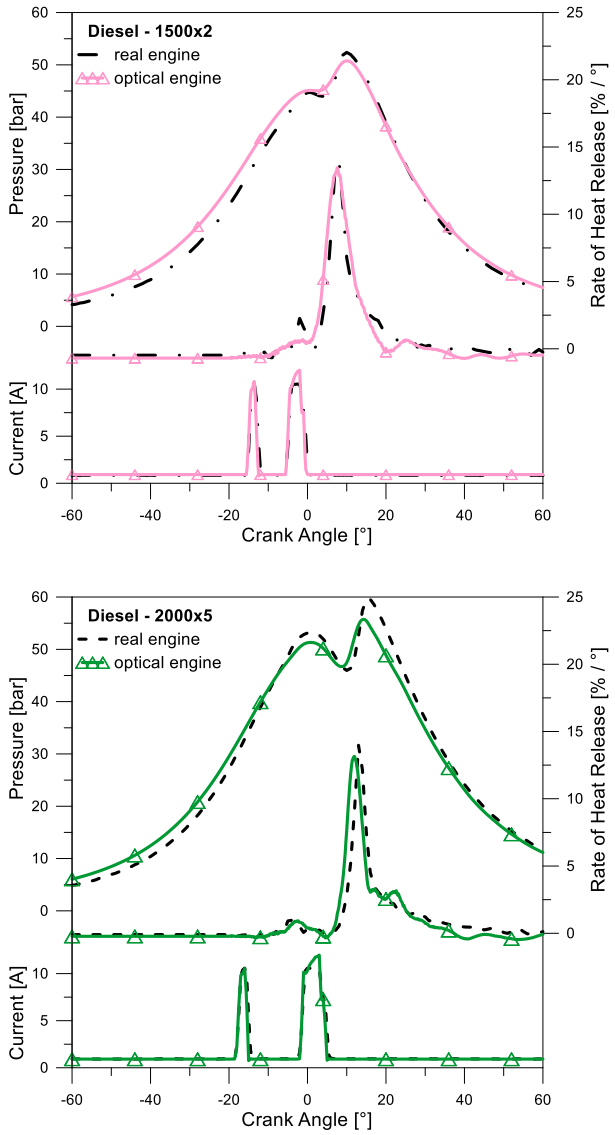

Figure 4. In-cylinder pressure, ROHR and injector current for diesel fuel at 1500x2 and 2000x5 in both real and optical engines.

Results and discussion

2d imaging in the visible and infrared spectrum has been performed in an optical diesel engine fed with commercial diesel fuel and two non-conventional fuels: RME and HG, a blend of diesel and a high glycerol content fuel. The work is divided in four sections: first, only commercial diesel is used and a comparison between two engine operating points is carried out to highlight the advantages of infrared imaging. Then, the results of the infrared imaging obtained with RME and HG are presented separately. Finally, the three fuels are compared in terms of infrared emission curves and cyclic variation.

1. Characterization of diesel fuel

The analysis of in-cylinder signals is useful to measure the combustion parameters. Analyzing the ROHR curve in Figure 4, the start of combustion (SOC) has been detected as the instant when the energy release begins to exceed the energy losses due to the fuel evaporating process [22]. At 1500x2, the SOC of the pilot and main injections occur at -10°CA and 0.5°CA, respectively. At 2000x5, they occur at -9°CA and 5°CA, respectively. On the other hand, optical engines give the advantage to obtain additional information about the combustion process through the direct visualization of the phenomena that take place inside the cylinder. 2d imaging during the injection and combustion phases has been performed in both the engine conditions of Figure 4. Moreover, two-color pyrometry technique has been applied to obtain the qualitative soot concentration. Figure 5 shows visible and processed images of the injection and combustion phases at 1500x2 and 2000x5 for diesel fuel. During the pilot injection, two lamps have been used to light the fuel jets. At 1500x2, the first luminous flames have been detected at the TDC (indicated as Start of visible combustion in Figure 5); since the main SOC occurs later, the flames are due to the pilot combustion that started at -10°CA. Hence, in the visible range it is not possible to detect the reactions that take place immediately after the SOC of the pilot. The same happens at 2000x5 where the first luminous flames can be detected at the TDC while the SOC of the pilot is at -9°CA. In this case, it is more evident that the flames are not due to the SOC of the main injection that occurs 5°CA later. The main combustion at 1500x2 is characterized by a two phases. In the first, the flames are localized on the jet axis; the fuel burns with very intense luminous emission and soot production, this phase is evident at 8°CA. Then, the flames distribute along the chamber wall, where additional fuel is supposed to be available for the combustion (from 16°CA to 20°CA). The luminous flames emission is visible until 40°CA (indicated as End of visible combustion), after this point no light is detectable from the combustion chamber. In the processed images, sharp gradients of the soot concentration have been detected because almost the whole area where soot appears is characterized by the maximum value of soot concentration (105 a.u.). Therefore, images with lower soot amount will be characterized by small soot regions. To reduce the local soot concentration, a more efficient mixing with the available air is required. Combustion behavior of the main injection at 2000x5 is different from the previous case because it is characterized by on-wall combustion with the formation of a hole in the center of the bowl. The combustion has a longer angular duration due to the higher engine speed. The last crank angle where luminous flames are still visible is 55°CA. Soot formation images are helpful to highlight the critical issues of this process. The ring shape observed in the visible images is well defined in the processed images (20°CA). Large soot regions are detectable and, as the previous case, the soot value is the maximum in almost the whole area. Due to the longer combustion duration, regions with low soot concentration can be detected in the expansion stroke up to 40°CA. During this phase, the oxygen in the cylinder reduces part of the soot previously formed. To overcome the limitations of optical diagnostic in the visible range, infrared imaging has been performed in the same engine conditions and a comparison of experimental results has been carried out.

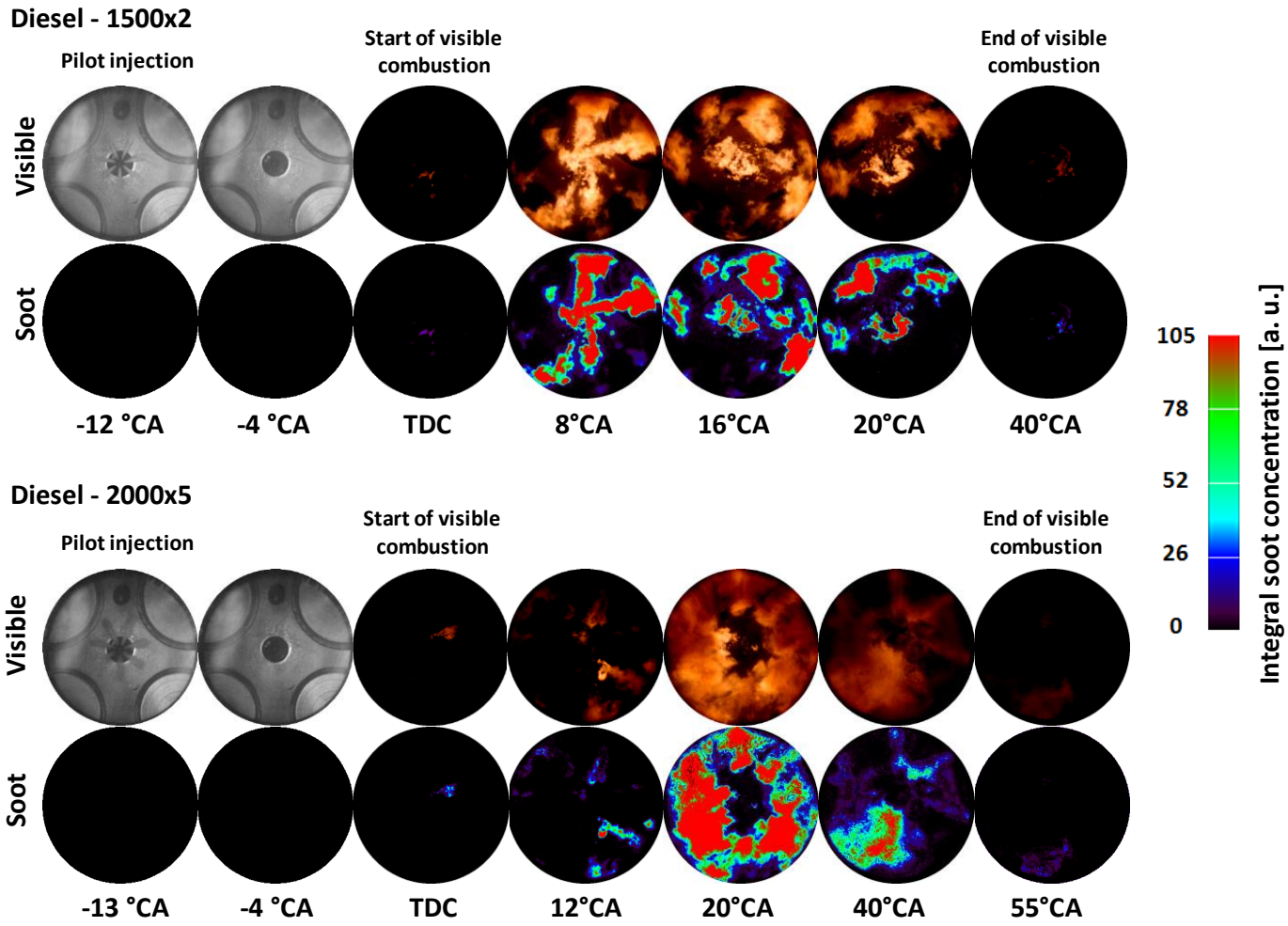

Figure 5. Imaging of injection and combustion processes in the visible range and soot concentration obtained by two-color pyrometry, for diesel fuel at 1500x2 and 2000x5.

Figure 6 reports a collection of images of injection and early combustion phase for diesel fuel at 1500x2. In the first row, images in the visible range have been reported while infrared images have been shown in the rows below. Beside the full infrared spectrum of the camera (1.5 – 5 µm with an attenuation of 10% - ND1 filter was used), images have been recorded using two band pass filter at 4.2 µm (emission wavelength of CO_2 molecule) [17] and at 3.9 µm (sensitive to alkyl C-H, aldehyde C-H, and acid OH) [18]. Infrared images have been presented using different color scale limits for each one in order to get the best visualization. The color scale is shown in Figure 6, black is for low values and white is for high values. Since the maximum and minimum values are not fixed, their numerical values have been reported for each image.

The first crank angle of Figure 6 corresponds to the end of pilot injection. After this point, no more fuel can be detected in the visible range. The combustion chamber appears empty until the main injection event that can be observed at the TDC. In contrast to the lack of information in the visible range between -9°CA and -3°CA, a lot of comments can be made looking at the infrared images. Using the ND1 filter a strong infrared emission in the location of the jet axis can be seen, it corresponds to the SOC of pilot injection (-10°CA) detected from the ROHR curve. Images show the injected fuel that reacts with in-cylinder gas, moves according to swirl motion (counterclockwise) and it spreads toward the chamber wall (images from -9°CA to -3°CA). A cloud seems to cover the reacting spray; the CO_2 emission of this cloud can be isolated using the filter at 4.2 µm. In the images of the third row, from -12°CA to -3°CA, a quite uniform cloud is visible and it represents the energy emitted by the recirculated exhaust gas at the end of the compression stroke. While the filter at 4.2 µm is sensitive to the CO_2 contained in the recirculated gas, the one at 3.9 µm can remove the radiation of the hot gas and point out the fuel location (HCs) and the intermediate products of the combustion. This filter has been useful to follow the evolution of the injected fuel after the end of injection. In the last row, from -12°CA to -3°CA, fuel that has not yet mixed with the available air is visible. From the TDC on, different phenomena occur and they need to be described individually. At the TDC, the main injection is penetrating in the combustion chamber as shown in the visible image in the first row. The infrared full spectrum shows hot gas that overlaps liquid fuel (detected in the visible images). At 3°CA, no more fuel can be detected from visible images as it was before for the pilot injection. However, high infrared emissions are detected in the second row due to the flames. Even if a strong infrared radiation is emitted from the gas (third row), the filter at 3.9 µm is still able to highlight the fuel that is reaching the chamber wall. At 6°CA and 9°CA, the visible images show that the flames are located on the jet axis.

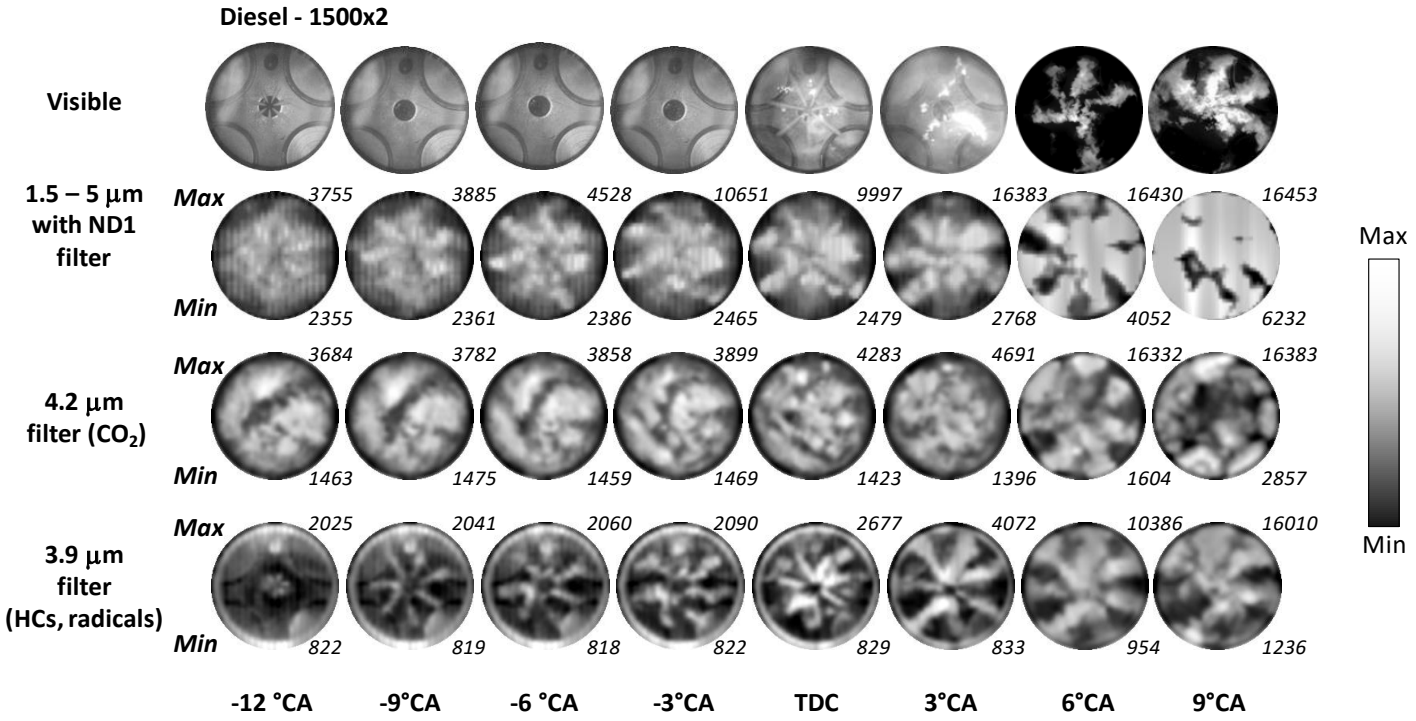

Figure 6. Images of injection phase and early combustion phase in the visible range (first row), in the full infrared range (second row), at 4.2 µm (third row) and at 3.9 µm (last row), for diesel fuel @1500x2.

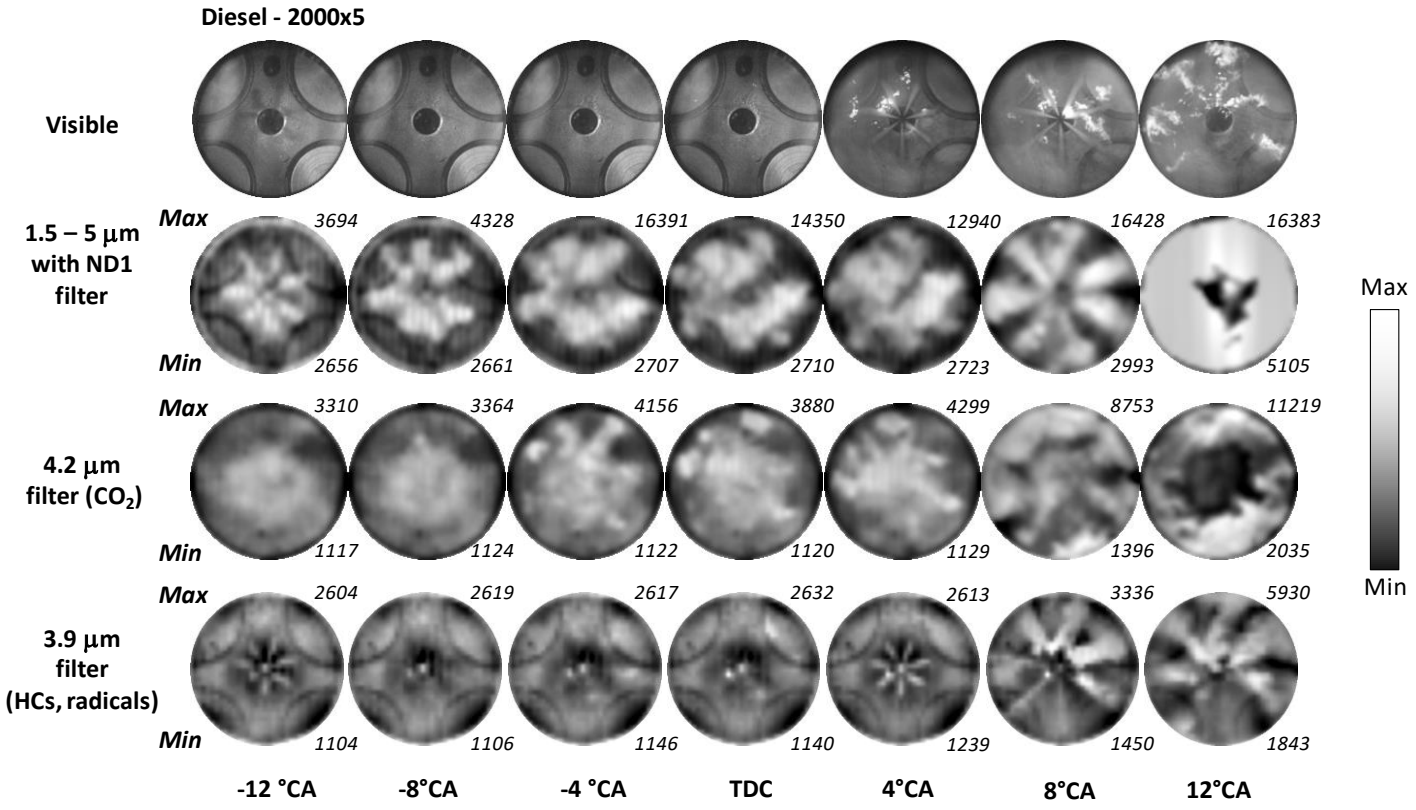

Figure 7. Images of injection phase and early combustion phase in the visible range (first row), in the full infrared range (second row), at 4.2 µm (third row) and at 3.9 µm (last row), for diesel fuel @2000x5.

While a huge quantity of energy is collected in the full IR spectrum, approaching the sensor saturation, two interesting comments can be made on the images at 4.2 µm and 3.9 µm. In the first, it is evident the formation of seven clouds along the chamber wall. This CO_2 cluster seems to be due to the heavy fuel impingement detectable from the images at 3.9 µm. At this wavelength, the seven jets assume the typical mushroom shape on the tip. After that the fuel reaches the chamber wall, it starts to diffuse in the circumferential way. The visualization of this phenomenon is very important since this information was not available from visible imaging. Similar considerations can be made analyzing the engine condition 2000x5. In Figure 7, a collection of images of injection and early combustion phase for diesel fuel has been reported. The four rows correspond to the visible range, the infrared full spectrum, the band pass filters at 4.2 µm, and at 3.9 µm, respectively. Since the camera frequency was kept to 3003 Hz, the higher engine speed involves an image resolution of 4°CA. As seen before, in the visible range, after the end of pilot injection no fuel can be detected in the combustion chamber and no evidence of the SOC of the pilot injection can be observed. The main injection is visible at 4°CA and 8°CA while only flames are observable at 12°CA. On the other hand, an intense emission can be detected in the full infrared spectrum. The spray reaction and the mixing with the in-cylinder gas can be seen from -12°CA to 0°CA. Image at 4°CA shows that the main injection penetrates across a cloud of gas and reacting spray, and finally it burns. Image with 3.9 µm filter at 8°CA highlights that the ignition is not the same for all the jets. The first reactions appear in the upper-right part of the combustion chamber. This agrees with the flames observed in the visible images. On the contrary, it could not be detected in the full spectrum images. Generally, the contour of the IR radiation with 3.9 µm filter identify in a reliable way the visible flames (9°CA @ 1500x2 and 12°CA @ 2000x5). Using the band pass filter at 4.2 µm the already seen mushroom formation has been noted when the fuel reaches the chamber wall (8°CA). Moreover, the CO_2 clouds at 12°CA assume the same ring shape that characterizes the visible flames in the following crank angles (see Figure 5).
Finally, in the images with 3.9 µm filter from -8°CA to 0°CA, unlike the previous case, no IR emission of HCs can be detected after the end of pilot injection. In this condition higher temperature and air flow in the cylinder promote the fuel/air mixing. No pilot combustion can be detected because of the small amount of injected fuel.

In order to get a complete vision of the infrared emission across all the engine strokes and for a quick comparison of the results obtained with different filters, the mean values of the infrared emission have been calculated for each image and they have been plotted versus the crank angle. As example, Figure 8 reports the infrared emission curve during the fired (solid line) and the motored (dashed line) conditions for diesel fuel at 2000x5 with the 4.2 µm filter. The curve relative to the CO_2 was chosen because of its intense emission during the most of the engine strokes; moreover, this filter is characterized by the highest peak value during the motored condition. In this condition, only fresh air flows in the cylinder and the infrared emission is due to the energy emitted by the air when it is compressed; its peak value corresponds to the TDC with closed valves. In order to get the net contribution of the exhaust gas recirculation, fuel injection, mixing, and combustion, the curve recorded in motored condition is subtracted to the one in fired condition. The result is the net curve in the bottom of Figure 8 (solid line with symbols); its minimum value passes across zero and its shape across the TDC is changed. The curve shows that there is no significant emission from recirculated exhaust gas during the intake phase (-360°CA -180°CA); on the contrary, they emit energy starting from -80°CA until the start of main combustion. Moreover, even higher emission intensity has been observed during the whole expansion and exhaust strokes.

Hereafter, for the analysis of different fuels, engine conditions, and optical configurations, only the net curves will be shown. Figure 9 reports the net curve of IR emission for the three filters, the ROHR curve and integral soot concentration obtained from the image processing using two-color pyrometry technique. The curves of IR emission have been obtained performing the ensemble average on 24 consecutive combustion cycles. More details about the cycle to cycle variation in the infrared range will be discussed later.

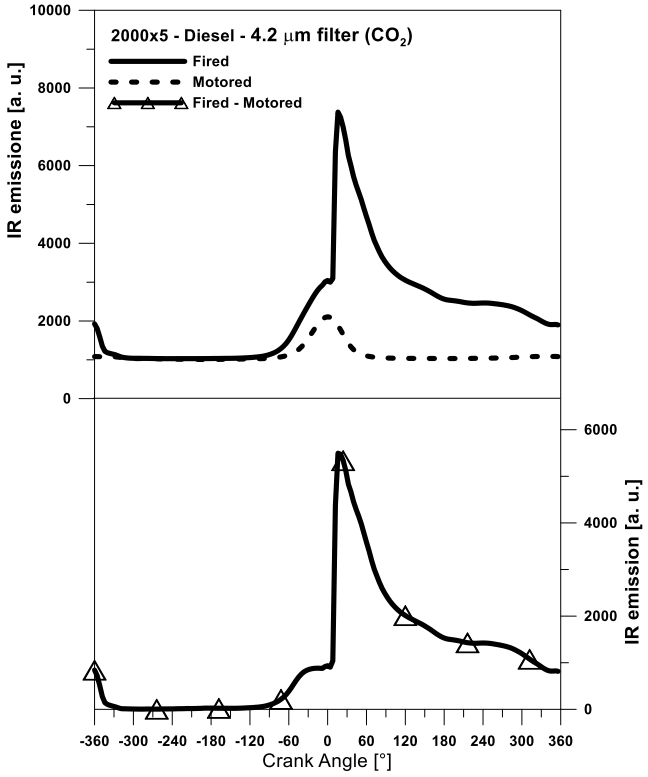

Figure 8. Average infrared emission versus crank angle in fired and motored conditions (top). Net curve (bottom).

At 1500x2 (Figure 9, top), the soot formation starts at 3°CA (gray square), before the peak of the ROHR curve at 8°CA. The start of soot formation corresponds to the start of IR emission at 4.2 µm and 3.9 µm (gray squares). The maximum soot formation occurs at 12°CA (gray triangle); it is aligned to the peaks of all the infrared curves. The IR emission in the range 1.5 - 5 µm starts at -2.5°CA (gray circle), that is before the start of visible combustion detected at the TDC. In addition, the curve shows an inflection at 3°CA that is the start of soot formation and of IR emission at 4.2 µm and 3.9 µm. Moreover, its raising part overlaps the ROHR trace. After the peak, all the curves decrease with different slope, however, they approach to the zero more slowly than the soot concentration curve. This is zero at 40°CA that is the end of visible combustion. At 2000x5 (Figure 9, bottom), the soot formation starts again before the peak of the ROHR that is at 12°CA. The soot formation starts at 8°CA (gray square) together with the IR emission at 3.9 µm while the IR emission at 4.2 µm starts at 4°CA (gray square). The peak of soot formation is aligned to the peaks of all the infrared curves and it is at 20°CA (gray triangle). The IR emission in the range 1.5 - 5µm starts at -5°CA (gray circle), that is before the start of visible combustion detected at the TDC. It has an inflection at 8°CA, after the start of main injection at 5°CA. The IR rising trace is delayed with respect to the ROHR curve.

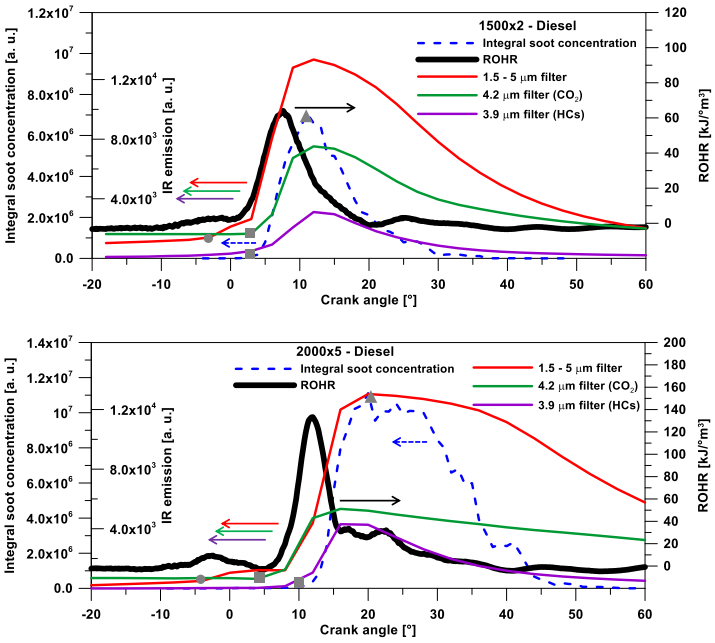

Figure 9. IR emission curves with three filters, ROHR and integral soot concentration for diesel fuel at 1500x2 and 2000x5.

Summarizing the observations about the IR emission curves in two engine points using diesel fuel, the IR emission in the full spectrum is always the most sensitive; it has the highest value and starts earlier than other curves. The second to start is the curve at 4.2 µm. It must be noted that it starts very early, at about -80°CA, due to the IR emission of intake burned gas mixed with fresh air. After, it increases again when combustion takes place.
IR emission at 3.9 µm rises when the soot formation starts. Since the two band pass filters just have the function to take a portion of the full IR radiation, the peak values of the three IR curves are aligned.
IR emission in the full spectrum is sensitive to energy variations before the start of visible combustion; moreover it is characterized by an inflection at approximately the SOC of main injection. At 3.9 µm, higher IR emission is detected at 1500x2 than at 2000x5 between -10°CA and TDC, this is correlated to the slower evaporation and reaction of the pilot injection at 1500x2.

2. *Characterization of RME fuel*

In order to verify the reliability of the optical diagnostic in the infrared band with a fuel different from commercial diesel, the same analysis has been made using the first generation biodiesel RME. As shown in Table 3, it has a lower Low Heating Value (LHV) while higher density, viscosity, Cetane Number (CN), and distillation temperature than diesel. Moreover it is a fuel with high oxygen content.

Figure 10 reports the in-cylinder signals at 1500x2 and 2000x5 for diesel and RME. In particular, the pressure signals, the calculated ROHR, and the injector current are shown. The injection strategy used for RME is derived from the real engine operated with a closed loop control on the IMEP and the combustion center. To take into account the lower LHV of RME, longer durations have been set for the main injection.
At 1500x2, the pressure value is the same during the compression stroke since the same intake pressure has been used. From the ROHR trace, the pilot and main SOC have been identified. They are the same as for the diesel fuel, the pilot SOC is at -10°CA while the main SOC is at 0.5°CA. The pilot combustion of RME is weaker than the diesel one; this produces a lower pressure at the TDC. Due to higher density and viscosity, RME is not able to mix efficiently for short injection duration [26]. The combustion of the main injection is faster and the maximum pressure of RME is higher than that of diesel. On the other hand, the combustion duration detected from the ROHR trace is shorter for RME. Similar considerations can be made at 2000x5. The SOC of the pilot and of the main are the same of diesel fuel. They occur at -9°CA and 5°CA, respectively. The weak combustion of pilot is compensated for by the intense main combustion. The high peak value of ROHR and the delayed position suggest that part of the pilot injection burns together with the main. Imaging of injection and combustion processes in both engine operating points has been performed for RME in the visible and infrared band.

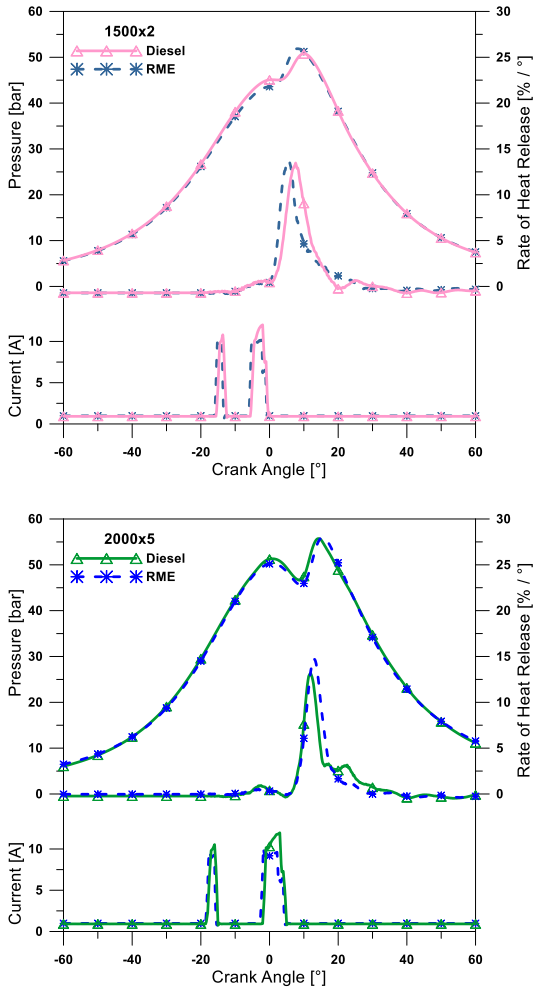

Figure 10. In-cylinder pressure, ROHR and injector current for diesel and RME fuels at 1500x2 and 2000x5 in the optical engine.

In Figure 11, the images relative to the visible range, the full infrared spectrum from 1.5 µm to 5 µm, the band pass filter at 4.2 µm and at 3.9 µm have been reported for the condition 2000x5. The angular interval is the same used for diesel fuel and it covers the end of pilot injection and the combustion of the main injection. While in the visible range, the only background of the combustion chamber can be detected at -12°CA and at -8°CA, the reacting spray can be observed in the full spectrum images.

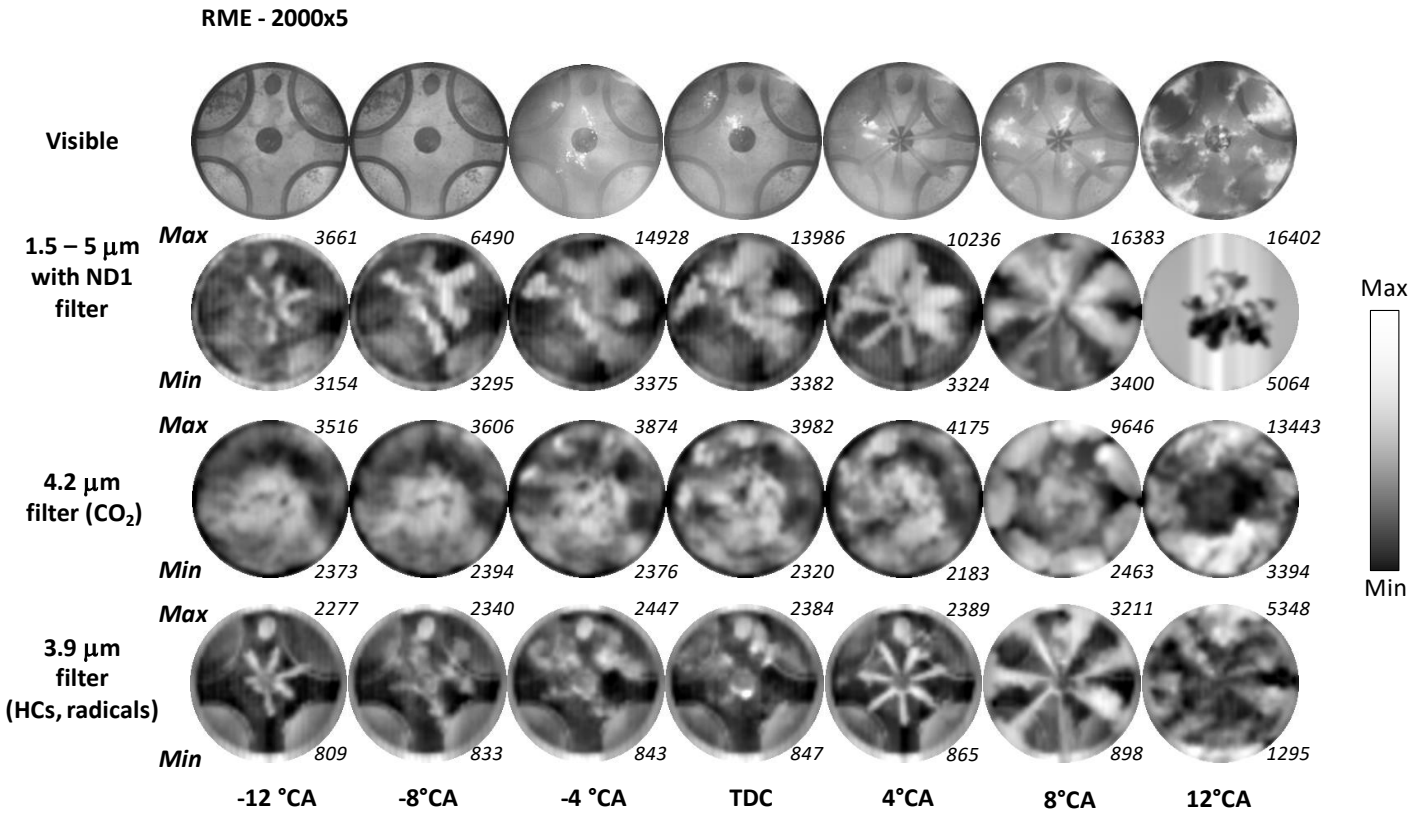

Figure 11. Images of injection phase and early combustion phase in the visible range (first row), in the full infrared range (second row), at 4.2 µm (third row) and at 3.9 µm (last row), for RME fuel @2000x5.

In particular, the IR emission seems to be due to a certain amount of RME fuel that doesn't mix with the air as efficiently as diesel does. This is due to RME higher distillation temperature, density, and viscosity. At the start of visible combustion, at -4°CA, some flames appear in the visible images and a wide cloud is observable in the IR images in 1.5 - 5 µm range. Some regions with HCs and products of intermediate reactions are visible from the image taken with the 3.9 µm filter. This is in agreement with the presence of flame spots in the visible images.

Analyzing the images at 4.2 µm from -12°CA to 0°CA, a circular gas cloud can be observed in the center while some local points with high intensity appear on the periphery. During the main injection (4°CA), the liquid fuel is injected in a cloud of reacting pilot spray and gas. Later, at 8°CA, the visible image shows flames on the jet boundary. These have been detected in the full IR spectrum where the mushroom shape of the jet and high emission levels on the boundary are evident. At 3.9 µm, the same mushroom shape has been detected without the influence of burning gas. In this instant, CO_2 clouds grow on the chamber wall as it was for diesel. Then, at 12°CA, these clouds distribute according to swirl motion and form a ring.

In Figure 12, the net curve of IR emission for the three filters, the ROHR curve and integral soot concentration have been reported in order to analyze the correlations between IR radiation and combustion parameters with RME. At 1500x2, the IR radiation in the full spectrum is able to detect the SOC of pilot injection; an inflection is evident at -10°CA (gray circle). Moreover, a second inflection is at approximately the TDC that is close to the SOC of the main injection (0.5°CA). As for diesel fuel, the raising part of the IR radiation in the full spectrum overlaps the ROHR trace after the main injection SOC. Also the curves relative to the band pass filters at 4.2 µm and 3.9 µm start at the TDC (gray squares). Unlike the previous case, for RME, they are in advance with respect to the start of soot formation, that is at 9°CA (gray square). This happens because in this case the soot formation starts later. The instant of maximum soot formation (gray triangle) is at 17°CA; it is delayed with respect to the peaks of IR emission curves that have been detected at 10°CA. Then, a second inflection is evident at the TDC that is in advance with respect to the SOC of the main injection (5°CA).

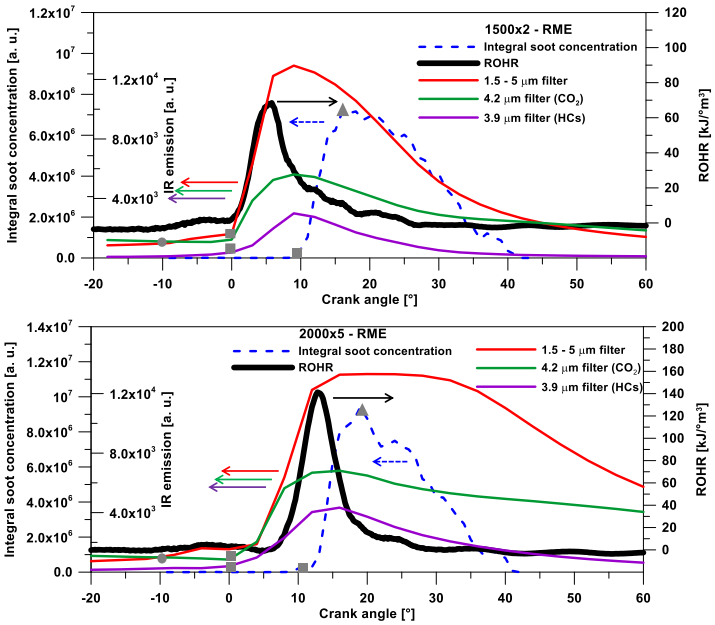

Figure 12. IR emission curves with three filters, ROHR and integral soot concentration for RME fuel at 1500x2 and 2000x5.

Due to this shift, the raising part of the curve does not fit the ROHR trace. In agreement with the IR emission in the full spectrum, also the signals at the two filtered bands start at the TDC (gray squares). Even in this case, they anticipate the start of soot formation (10°CA). Finally, the maximum soot formation (gray triangle) occurs shortly after the peak values of IR emission curves.

3. *Characterization of HG fuel*

The last tested fuel is characterized by high glycerol content; in particular it is a blend of diesel (80% v/v) and high glycerol content fuel (20% v/v). The blend has been denoted as HG. It has higher density and viscosity while lower LHV, CN, and distillation temperature with respect to diesel. For this fuel, only the engine condition 2000x5 has been. In Figure 13, the in-cylinder signals for diesel and HG have been reported. In particular, the pressures signal, the calculated ROHR, and the injector current are shown. The same injection strategy has been used for both the fuels and a good agreement between the ROHR trace has been obtained. The SOC of both the pilot and main injections have been detected from the ROHR trace at -9°CA and 5°CA, respectively. The pilot combustion is not much efficient; it releases lower heat than the diesel one. This can be ascribed to both lower CN and LHV. On the other hand, the combustion of the main injection is stronger than the diesel one and this is likely due to a portion of the pilot injection that takes part to the combustion. The heat release peak of HG is higher and delayed with respect to the diesel one. This produces high peak pressure. In the late combustion phase, HG has lower heat release rate and its combustion duration is shorter than for diesel. In-cylinder processes have been investigated also by means of optical diagnostic. A collection of images recorded during the injection and combustion phases have been reported in Figure 14. Starting from the top, the four rows refer to visible range, infrared band from 1.5 to 5 μm, infrared wavelength at 4.2 μm, and at 3.9 μm, respectively. Mainly the same behavior of diesel and RME fuels has been observed. Reacting spray is detectable in the IR range while no evidence of fuel activity can be noted in the visible range. However, a few differences must be commented. In the range 1.5 to 5 μm, at 8°CA, HG shows more distributed emission intensity. On the contrary, it was located mainly along the jet axis for diesel and RME. At 4.2 μm wavelength, the ring shape of the gas cloud observed at 12°CA for the previous fuels appears at the TDC when using HG. There is no formation of isolated clouds when fuel impinges the wall (8°CA) but a more homogeneous gas cloud.

These observations are likely related to the lower boiling temperature of HG and then to the presence of a greater amount of evaporated fuel. Finally, at 3.9 μm some fuel plumes are evident after the end of pilot injection. In the analysis of diesel and RME, these liquid plumes were ascribed to the higher boiling temperature, density and viscosity of RME fuel. In this case, even if HG has the lowest boiling temperature, it is very close to that of diesel. On the other hand, its density and viscosity values are slightly higher than the diesel ones. The detection of HCs in the images from -12°CA to TDC suggests that the density and viscosity of the fuel play the main role in the fuel evaporation and then affect the mixture formation process.

In Figure 15, the same comparison showed for diesel and RME is presented. The net curve of IR emission for the three filters, the ROHR curve and integral soot concentration have been reported. The soot formation starts at 8°CA, before the peak of the ROHR curve (13°CA). Also the curves at 3.9 μm and 4.2 μm start at 8°CA (gray square). The curve of the full IR range starts at -10°CA (gray circle) that is the SOC of the pilot injection; it has a local peak at the TDC and an inflection at 5°CA that is the SOC of the main injection. A third inflection is detectable at 8°CA when also the other curves start. The maximum IR radiation can be detected at about 20°CA that is close to the peak of soot formation at 18°CA (gray triangle). Finally, as noted for the diesel fuel at 2000x5 (figure 9, bottom); also for HG fuel the rising part of the IR curve in the full spectrum is delayed with respect to the ROHR rising trace.

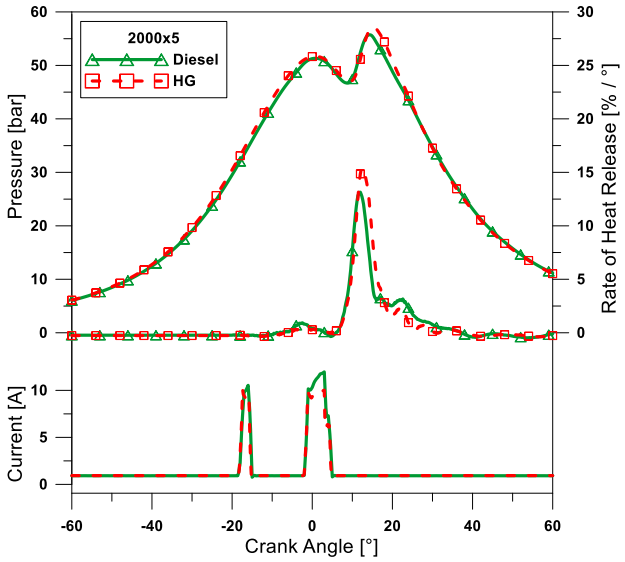

Figure 13. In-cylinder pressure, ROHR and injector current for diesel and HG fuels at 2000x5 in the optical engine.

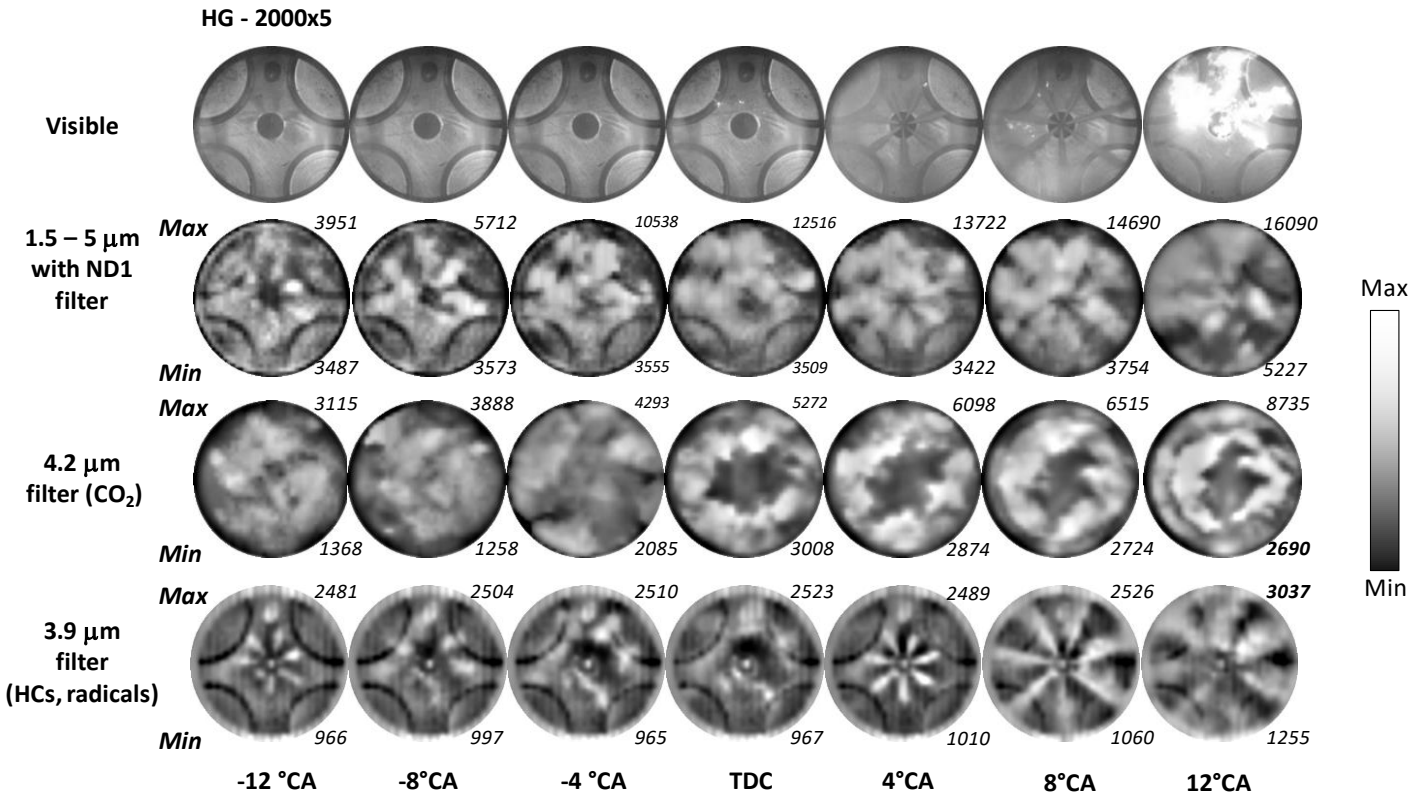

Figure 14. Images of injection phase and early combustion phase in the visible range (first row), in the full infrared range (second row), at 4.2 µm (third row) and at 3.9 µm (last row), for HG fuel @2000x5.

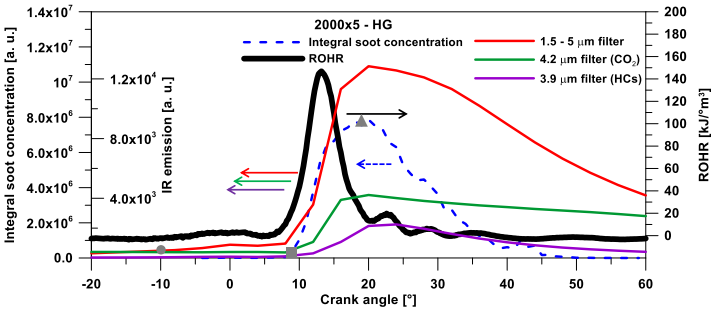

Figure 15. IR emission curves with three filters, ROHR and integral soot concentration for HG fuel at 1500x2 and 2000x5.

4. *Comparison between diesel, RME and HG*

4.1 Analysis of the data dispersion

The curves of IR emission have been obtained performing the ensemble average on 24 consecutive combustion cycles. A quantitative analysis of the dispersion of experimental data has been carried out through the evaluation of the coefficient of variation (CV) of the curves. It is defined as the ratio between the standard deviation and the mean value of the several tests performed. For the calculation of the CV, the curves relative to the fired condition has been used instead of the net curves (see Figure 8) because if the mean value is close to zero, the CV approaches to infinity and its value is no longer significant.

The maximum value of the CV has been measured in order to gives information about the critical phases of the combustion process, the filtering and the fuel effect. In Table 6, the maximum values of the CV have been reported for all the investigated fuels in the engine condition 2000x5 for the three optical configurations. The highest dispersions have been noted for the images recorded in the full IR spectrum of the camera. In this range, the maximum sensitivity is obtained and then differences among cycles are highlighted. On the other hand, CV is lower when the band pass filters at 4.2 µm and 3.9 µm are used. The analysis between the fuels has shown that the maximum dispersion (CV =0.37) is obtained for the RME fuel that is the one with the highest CN. Data dispersion of IR curves for RME is shown in Figure 16. Also in [12], the fuel with the highest CN had the highest CV; however, the CV of RME was lower than the diesel one. This mismatch is ascribed to the high data dispersion in [12] (CV spanned from 0.58 to 0.84) with respect to the present work (CV spans from 0.25 to 0.37). The crank angle of the maximum CV has been reported in Table 6. It is mainly between 8°CA and 12°CA. It corresponds to the early combustion phase when the rate of heat release has a sudden increase. Here, the amount of detectable IR radiation is strictly linked to the progress of chemical reactions and then it is the point mostly affected by cyclic variation. Finally, a good repeatability of the measurements has been observed for all the tests.

Table 6. Analysis of the Coefficient of Variation of the IR radiation curves for all the investigated fuels at 2000x5.

Fuel	OP	Filter	CVmax	°CA of CVmax
Diesel	2000x5	ND1	0.31	12
Diesel	2000x5	4.2	0.20	8
Diesel	2000x5	3.9	0.22	12
HG	2000x5	ND1	0.25	12
HG	2000x5	4.2	0.18	12
HG	2000x5	3.9	0.11	16
RME	2000x5	ND1	0.37	8
RME	2000x5	4.2	0.25	4
RME	2000x5	3.9	0.27	8
OP: Operating Point ***CV: Coefficient of Variation***				

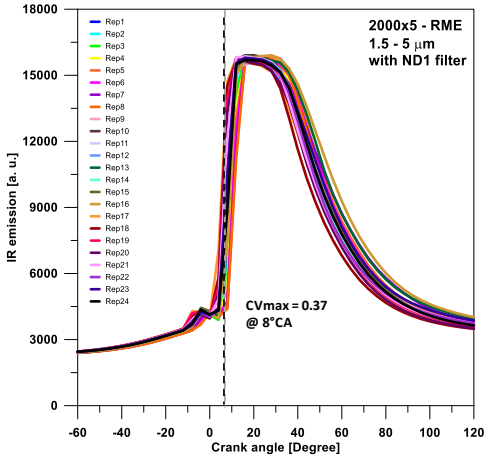

Figure 16. Curves of IR emission in the full range with ND1 filter for 24 consecutive repetitions. RME fuel at 2000x5.

4.2 Analysis of the infrared emission curves

Besides the comparison between the IR emission curves, the ROHR and the soot concentration for the investigation of the combustion parameters, the analysis of the mean IR radiation for different fuels can highlight the effect of fuels properties. In Figure 17, the IR emission curves for the three optical configurations have been reported for diesel and RME at 1500x2.

The IR emission curve in the full range with ND1 for the RME starts slightly in advance and decreases earlier than the one of the diesel. This behavior is correlated to the ROHR of the two fuels. In fact, as noted in Figures 9 and 12, for both diesel and RME, the rising part of the IR emission curve in the full range with ND1 fits the ROHR trace. The ROHR trace for RME increases faster and decreases earlier than the diesel one (Figure 10). From the curves in the middle in Figure 17, the amount of CO_2 in the combustion chamber seems to be grater for the diesel both in the late compression phase and at the peak of IR emission. Also in the curves recorded with the band pass filter at 3.9 µm (Figure 17, bottom), the RME is in advance with respect to the diesel. Since these differences appear after the TDC, they are ascribed to the detection intermediate products of the combustion since high radiations have been detected also in the full spectrum.

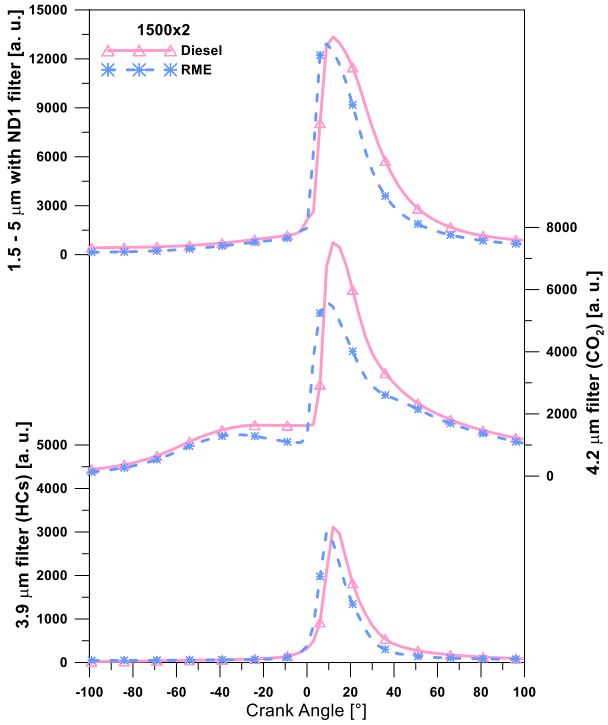

Figure 17. Comparison of IR emission curves for diesel and RME at 1500x2.

The IR emission curves for the three optical configurations, for all the tested fuels at 2000x5, have been reported in Figure 18. Analyzing the IR radiation from 1.5 µm to 5 µm, different behaviors can be observed for RME and HG with respect to diesel. IR emissions for HG and diesel start together but the HG decreases earlier. This is in agreement with the ROHR curves of the two fuels observed in Figure 13. On the other hand, the IR emission of RME starts in advance even if the ROHR trace of RME overlaps the diesel and HG one during the rising phase. This effect is not well understood, however it could be due to the fuel properties in this particular engine operating point. In fact, at 1500x2, the IR emission of RME started together with the diesel one and it was in agreement with ROHR evolution (Figures 10 and 17). Also the decreasing part of the RME curve in the full spectrum is unclear. The ROHR of RME overlaps the one of HG in this condition. On the contrary, the IR emission curve for RME descends along with the diesel one.

The curves of IR emission at the wavelength of 4.2 µm show that RME has the highest value and the HG has the lowest one. The diesel is in the middle. The lack of a clear trend in the CO_2 detection could be due to the different spatial distributions observed for the three fuels.

When the band pass filter at 3.9 µm is used, the first fuel to emit at this wavelength is RME. Its radiation starts at the TDC while diesel and HG emissions are visible at 8°CA. These differences are ascribed to the distillation temperature, density and viscosity of the fuels. RME has the highest value. Moreover, a significant difference at the peak value can be observed between the fuels, in particular the peak of HG curve is half that of diesel and RME.

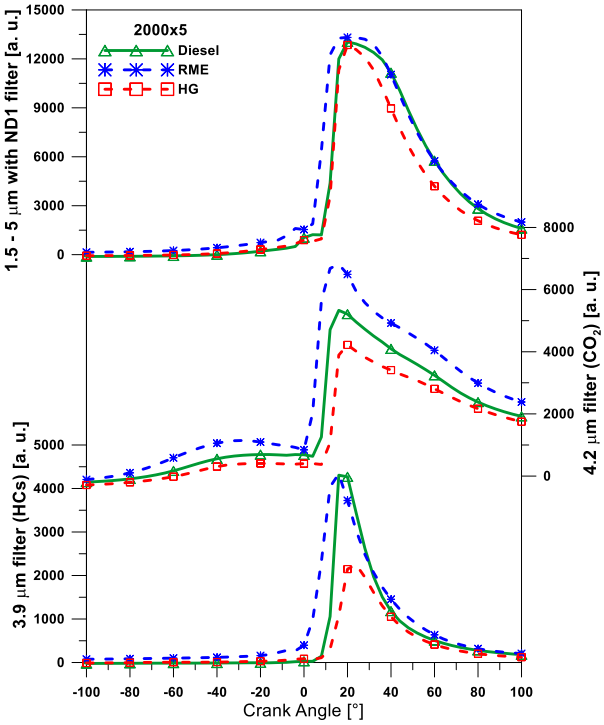

Figure 18. Comparison of IR emission curves for diesel, RME and HG at 2000x5.

Summary/Conclusions

Infrared imaging has been performed in an optical engine to investigate the behavior of different fuels. Commercial diesel fuel and two non-conventional fuels have been used to run two engine operating points of the NEDC characterized by double injection strategies. The non-conventional fuels are RME and an experimental blend (HG) of diesel and a fuel with high glycerol content. The in-cylinder behavior of these fuels has been investigated in the infrared range from 1.5 to 5 µm; moreover, two band pass filters at 4.2 and at 3.9 have been used.

The IR imaging has confirmed to be sensitive in a wider angular range than the visible diagnostic. Reactions immediately after the SOC of the pilot injection and after the end of visible combustion can be detected in the IR band. The peak of IR emission corresponds to the peak of soot formation. The fuel impingement can be visualized despite of the visible imaging. The filter at 4.2 µm can detect the in-cylinder CO_2 produced during the combustion. Emission at 3.9 µm highlights the location of HCs and the products of intermediate reactions.

After the pilot injection, images of HCs locations for diesel have shown that a faster air/fuel mixture is obtained at the highest engine load. RME and HG are characterized by a less efficient air/fuel mixture than diesel because of their high density and viscosity.
The slight advance of RME with respect to diesel in the emission curves at 3.9 µm denotes that the formation of intermediate products of combustion occurs earlier for RME. This agrees with its higher CN. Diesel and RME are characterized by the formation of isolated clouds of CO_2 near the chamber wall. A homogeneous gas cloud has been observed for HG likely because of its low boiling temperature.

The use of a band pass filter can reduce the data dispersion but it lowers the sensitivity to the cycle to cycle variations. The high CN of RME causes large cycle to cycle variations in the early combustion phase that produced the highest CV.

References

[1] R. O. Dunn and G. Knothe, “Alternative diesel fuels from vegetable oils and animal fats,” Journal of oleo science, vol. 50, no. 5, pp. 415–426, 2001.

[2] S. Imran, D. Emberson, D. Wen, A. Diez, R. Crookes, and T. Korakianitis, “Performance and specific emissions contours of a diesel and rme fueled compression-ignition engine throughout its operating speed and power range,” Applied Energy, vol. 111, pp. 771–777, 2013.

[3] A. Hassaneen, A. Munack, Y. Ruschel, O. Schroeder, and J. Krahl, “Fuel economy and emission characteristics of gas-to-liquid (gtl) and rapeseed methyl ester (rme) as alternative fuels for diesel engines,” Fuel, vol. 97, pp. 125–130, 2012.

[4] J.-H. Ng, H. K. Ng, and S. Gan, “Characterisation of engine-out responses from a light-duty diesel engine fuelled with palm methyl ester (pme),” Applied Energy, vol. 90, no. 1, pp. 58–67, 2012.

[5] B. Tompkins, H. Song, J. Bittle, and T. Jacobs, “Efficiency considerations for the use of blended biofuel in diesel engines,” Applied Energy, vol. 98, pp. 209–218, 2012.

[6] S. K. Hoekman and C. Robbins, “Review of the effects of biodiesel on nox emissions,” Fuel Processing Technology, vol. 96, pp. 237–249, 2012.

[7] N. Rahmat, A. Z. Abdullah, and A. R. Mohamed, “Recent progress on innovative and potential technologies for glycerol transformation into fuel additives: a critical review,” Renewable and Sustainable Energy Reviews, vol. 14, no. 3, pp. 987–1000, 2010.

[8] D. Gonzalez, W. Piel, T. Asmus, W. Clark, J. Garbak, E. Liney, M. Natarajan, D. W. Naegeli, D. Yost, E. A. Frame, J. P. Wallace et al., “Oxygenates screening for advancedpetroleum-based diesel fuels: Part 2. the effect of oxygenate blending compounds on exhaust emissions,” SAE Technical Paper 2001-01-3632, doi:10.4271/2001-01-3632, Tech. Rep., 2001.

[9] M. Jansons, S. Lin, and K. Rhee, “Infrared spectral analysis of engine preflame emission,” International Journal of Engine Research, vol. 9, no. 3, pp. 215–237, 2008.

[10] L. Dombrovsky, S. Sazhin, S. Mikhalovsky, R. Wood, and M. R. Heikal, “Spectral properties of diesel fuel droplets,” Fuel, vol. 82, no. 1, pp. 15–22, 2003.

[11] E. Mancaruso, L. Sequino, and B. M. Vaglieco, “IR imaging of premixed combustion in a transparent Euro5 diesel engine,” SAE Technical Paper 2011-24-0043, doi:10.4271/2011-24-0043, 2011.

[12] E. Mancaruso, L. Sequino, and B. M. Vaglieco, “GTL (Gas To Liquid) and RME (Rapeseed Methyl Ester) combustion analysis

in a transparent CI (compression ignition) engine by means of IR (infrared) digital imaging," Energy, vol. 58, pp. 185–191, 2013.

[13] E. Mancaruso, L. Sequino, and B. M. Vaglieco, "IR digital imaging for analysing in-cylinder combustion process in transparent diesel engine," in Photonics Technologies, 2014 Fotonica AEIT Italian Conference on. IEEE, 2014, pp. 1–4.

[14] R. L. Pecsok L. D. Shields, Modern Methods of Chemical Analysis, Wiley, New York, 1968.

[15] D. Pavia, G. Lampman, G. Kriz, and J. Vyvyan, Introduction to spectroscopy. Cengage Learning, 2008.

[16] E. Mancaruso and B. M. Vaglieco, "Premixed combustion of GTL and RME fuels in a single cylinder research engine," Applied Energy, vol. 91, no. 1, pp. 385–394, 2012.

[17] R. Ochoterena, M. Larsson, S. Andersson, and I. Denbratt, "Optical studies of spray development and combustion characterization of oxygenated and Fischer-Tropsch fuels," SAE Technical Paper 2008-01-1393, doi:10.4271/2008-01-1393, 2008.

[18] C. Beatrice, G. Di Blasio, M. Lazzaro, C. Cannilla, G. Bonura, F. Frusteri, F. Asdrubali, G. Baldinelli, A. Presciutti, F. Fantozzi et al., "Technologies for energetic exploitation of biodiesel chain derived glycerol: Oxy-fuels production by catalytic conversion," Applied Energy, vol. 102, pp. 63–71, 2013.

[19] D. R. Lide, CRC handbook of chemistry and physics. CRC press, 2004.

[20] U. Aronsson, C. Chartier, U. Horn, Ö. Andersson, B. Johansson, and R. Egnell, "Heat release comparison between optical and all-metal HSDI diesel engines," SAE Technical Paper 2008-01-1062, doi:10.4271/2008-01-1062, 2008.

[21] W. F. Colban, D. Kim, P. C. Miles, S. Oh, R. Opat, R. Krieger, D. Foster, R. P. Durrett et al., "A detailed comparison of emissions and combustion performance between optical and metal single-cylinder diesel engines at low temperature combustion conditions," SAE International Journal of Fuels and Lubricants, vol. 1, no. 1, pp. 505–519, 2009.

[22] J. B. Heywood, Internal combustion engine fundamentals. McGraw-Hill New York, 1988, vol. 930.

[23] ThermoVision Advanced – Addendum to Visioscope v1.2. Copyright 2004 by AVL List GmbH, Graz – Austria.

[24] R. Karinen and A. Krause, "New biocomponents from glycerol," Applied Catalysis A: General, vol. 306, pp. 128–133, 2006.

[25] U. Aronsson, H. Solaka, G. Lequien, O. Andersson, and B. Johansson, "Analysis of errors in heat release calculations due to distortion of the in-cylinder volume trace from mechanical deformation in optical diesel engines," SAE International Journal of Engines, vol. 5, no. 4, pp. 1561–1570, 2012.

[26] E. Mancaruso, L. Sequino, B. M. Vaglieco, C. Ciaravino, and A. Vassallo, "Spray formation and combustion analysis in an optical single cylinder engine operating with fresh and aged biodiesel," SAE International Journal of Engines, vol. 4, no. 1, pp. 1963–1977, 2011.

Contact Information

Ezio Mancaruso
Istituto Motori - Consiglio Nazionale delle Ricerche
Via G. Marconi, 4 - 80125 Napoli (Italy)
e.mancaruso@im.cnr.it
http://www.im.cnr.it

Luigi Sequino
Istituto Motori – Consiglio Nazionale delle Ricerche
Via G. Marconi, 4 - 80125 Napoli (Italy)
l.sequino@im.cnr.it
phone: +39-081-7177-185

Acknowledgments

The authors would like to thank Mr. Carlo Rossi and Mr. Bruno Sgammato for the engine assembly and for the support in the experimental activity.

Definitions/Abbreviations

°CA	Crank Angle Degree
2d	two-dimensional
BDC	Bottom Dead Center
BMEP	Brake Mean Effective Pressure
CCD	Charge Coupled Device
CI	Compression Ignition
CN	Cetane Number
CO	Carbon monoxide
CO_2	Carbon dioxide
CR	Compression Ratio
CV	Coefficient of Variation
ECU	Electronic Control Unit
EGR	Exhaust Gas Recirculation
ET	Energizing Time
OP	Operating Point

H/C	Hydrogen - Carbon ratio
HC	Hydrocarbon
HG	High Glycerol (fuel)
ICE	Internal Combustion Engine
IMEP	Indicated Mean Effective Pressure
IR	Infrared
LHV	Low Heating Value
ND1	Neutral Density with 10% attenuation
NEDC	New European Driving Cycle
NOx	Nitrogen Oxides
PM	Particulate matter
RME	Rapeseed Methyl Ester
ROHR	Rate Of Heat Release
SOC	Start Of Combustion
SOI	Start Of Injection
TDC	Top Dead Center